

Chern numbers hiding in time-of-flight images

Erhai Zhao^{1,2}, Noah Bray-Ali², Carl J. Williams², I. B. Spielman² and Indubala I. Satija^{1,2}

¹*Department of Physics and Astronomy,*

George Mason University, Fairfax, VA 22030 and

²*Joint Quantum Institute, National Institute of Standards and
Technology and University of Maryland, Gaithersburg, MD 20899*

(Dated: May 16, 2022)

Abstract

We present a novel technique for detecting topological invariants – Chern numbers – from time-of-flight images of ultra-cold neutral atoms. The Chern number of fermions in a lattice potential depends on magnetic field (for neutral atoms, generated by an artificial magnetic field) and the chemical potential; we find that the Chern numbers leave their fingerprints as oscillations in the atoms' momentum distribution. The signature is strikingly enhanced for anisotropic hopping, where we show the momentum distribution assumes a sinusoidal form with period determined by the Chern number.

PACS numbers: 03.75.Ss,03.75.Mn,42.50.Lc,73.43.Nq

Topological insulators (TI) are bohemian forms of quantum matter that insulate in the bulk but conduct on their edges or surfaces. TI states with same symmetry are distinguished from each other by topological invariants [1, 2]. For example, integer quantum Hall states of two-dimensional electron systems (2DES), are characterized by integer valued topological invariants, Chern numbers, which capture global properties of all occupied bands, and describe the Hall conductivity [3, 4]. In cold atom systems, it is an open problem to first create topological matter and then measure the resulting topological invariants [5]. We show that the Chern number of a lattice-quantum Hall system leaves its fingerprints in the system's momentum distribution, a simple second order correlation function and an everyday observable in cold-atom experiments.

Ultracold atom experiments are positioned to explore topological phases of matter in new parameter regimes, and with new detection techniques. For example, with the invention of synthetic gauge fields [6], the quantum Hall effect of bosonic atoms, fermions in non-Abelian gauge fields, and quantum spin Hall effect are all within reach [7]. In cold atoms systems, the interaction strength, lattice anisotropy, spin-orbit coupling [8], and even disorder are amenable to control, allowing easy access to phenomena unreachable in 2DES. In addition, cold atoms offer new measurement opportunities, including the straightforward detection of momentum distributions by imaging the atomic density after a time-of-flight (TOF). A dream for cold atoms experiments is to reveal the topological invariants directly, unmarred by the complexity of interpreting transport measurements.

Motivated by these developments, we revisit integer quantum Hall states of fermions in a 2D square lattice and show that their Chern numbers c_r are made manifest as oscillations in the momentum distribution $n(\mathbf{k})$ as measured in TOF images. The number of these oscillations in the lowest Brillouin zone (BZ) are equal to the Chern number. Importantly, the oscillations become more pronounced for anisotropic lattices where the hopping along the elementary lattice vectors \mathbf{e}_x and \mathbf{e}_y are different. Structure in the momentum distribution can thus be used to unambiguously resolve the topological invariants of a quantum Hall state and we provide a formal framework connecting the momentum distribution and topological invariants for anisotropic lattices.

Figure 1a shows where this structure is most evident in the magnetic field-hopping anisotropy plane: in the continuum limit (Fig. 1b) or for highly anisotropic lattices (Fig. 1c). The continuum limit can be understood from properties of Landau levels: the momentum distribution simply results from harmonic oscillator wavefunctions. In the anisotropic limit, states with energy at the band edges are dimerized: their localized wave functions are peaked at pairs of spatially separated

lattice sites. The size of these ‘‘Chern-dimers,’’ in units of the lattice spacing d , is equal to the Chern number associated with the corresponding band gap. Consequently, the single particle two-point correlation function [defined in Eq. (9)] is sharply peaked at a spatial separation equal to the dimer size, and the momentum distribution varies sinusoidally (Fig. 1c) with a period determined by the Chern number. This general structure has been numerically verified for isotropic lattices at large flux, but with reduced visibility.

We consider the Hofstadter model [9] of spinless fermionic atoms on a square optical lattice in the \mathbf{e}_x - \mathbf{e}_y plane

$$H = - \sum_{\langle \mathbf{s}, \mathbf{s}' \rangle} t_{\mathbf{s}, \mathbf{s}'} (e^{i\theta_{\mathbf{s}, \mathbf{s}'}} f_{\mathbf{s}}^\dagger f_{\mathbf{s}'} + \text{h.c.}) - \sum_{\mathbf{s}} \mu_{\mathbf{s}} f_{\mathbf{s}}^\dagger f_{\mathbf{s}}. \quad (1)$$

Here, $f_{\mathbf{s}}^\dagger$ is the creation operator for a fermion at site $\mathbf{s} = \{s_x, s_y\}$; the nearest-neighbor hopping strengths $t_x = t_{\mathbf{s}, \mathbf{s}+\mathbf{e}_x}$, and $t_y = t_{\mathbf{s}, \mathbf{s}+\mathbf{e}_y}$ are real and positive; $\theta_{\mathbf{s}, \mathbf{s}'} = e \int_{\mathbf{s}}^{\mathbf{s}'} \mathbf{A} \cdot d\mathbf{l}$ depends on the vector potential \mathbf{A} [18] for particles with charge e ; and $\mu_{\mathbf{s}}$ is a local chemical potential. With cold atoms, the hopping anisotropy $\lambda = t_y/t_x$ can be tuned by varying the intensity of the lasers giving rise to the optical lattice potential [6]. $\alpha = d^2 e B / h$ is the magnetic flux per plaquette in units of the flux quantum. We study homogeneous gasses with $\mu_{\mathbf{s}} = \mu$, and also finite systems in the presence of an isotropic harmonic trap potential, captured by $\mu_{\mathbf{s}} = \mu_0 - m\omega^2 d^2 \mathbf{s}^2 / 2$.

Artificial magnetic fields have been implemented for bosons [10], and it is straightforward to apply these techniques to fermions. With their smaller fine-structure splittings, the alkali fermions (^6Li and ^{40}K) are more susceptible to heating from spontaneous emission than some bosons (^{87}Rb and ^{133}Cs), but for the $\hbar/t_{x,y} \sim 240 \mu\text{s}$ timescales [19] associated with the major energy gaps in the spectrum (see Fig. 2a), the expected ≈ 200 ms lifetime in ^{40}K should be acceptable; see Ref. [11] for an alternate solution.

We first summarize the well known properties of the homogeneous Hofstadter model [Eq. (1)] with commensurate flux $\alpha = p/q$, where the integers p, q are relatively prime. In the Landau gauge suitable for current experiments [6], the vector potential $\mathbf{A} = \alpha x \mathbf{e}_y$ scales the unit cell along \mathbf{e}_x by a factor of q to a magnetic unit cell; this also creates a magnetic Brillouin zone (MBZ) with $k_x \in (-\pi/q, \pi/q]$ and $k_y \in (-\pi, \pi]$. The Hofstadter model is diagonal in the single-particle basis $\Psi_{s_x, s_y} = e^{i(k_x s_x + k_y s_y)} \psi_{s_x}(k_y)$, provided ψ_{s_x} satisfies [9]

$$e^{ik_x} \psi_{s_x+1}^r + e^{-ik_x} \psi_{s_x-1}^r + 2\lambda \cos(2\pi s_x \alpha + k_y) \psi_{s_x}^r = -E_r \psi_{s_x}^r \quad (2)$$

with energy in units of t_x . The index $r = 1, 2, \dots, q$ labels linearly independent solutions, and $\psi_{s_x+q}^r = \psi_{s_x}^r$. The single energy band at $\alpha = 0$ splits into q sub-bands, and the energy spectrum

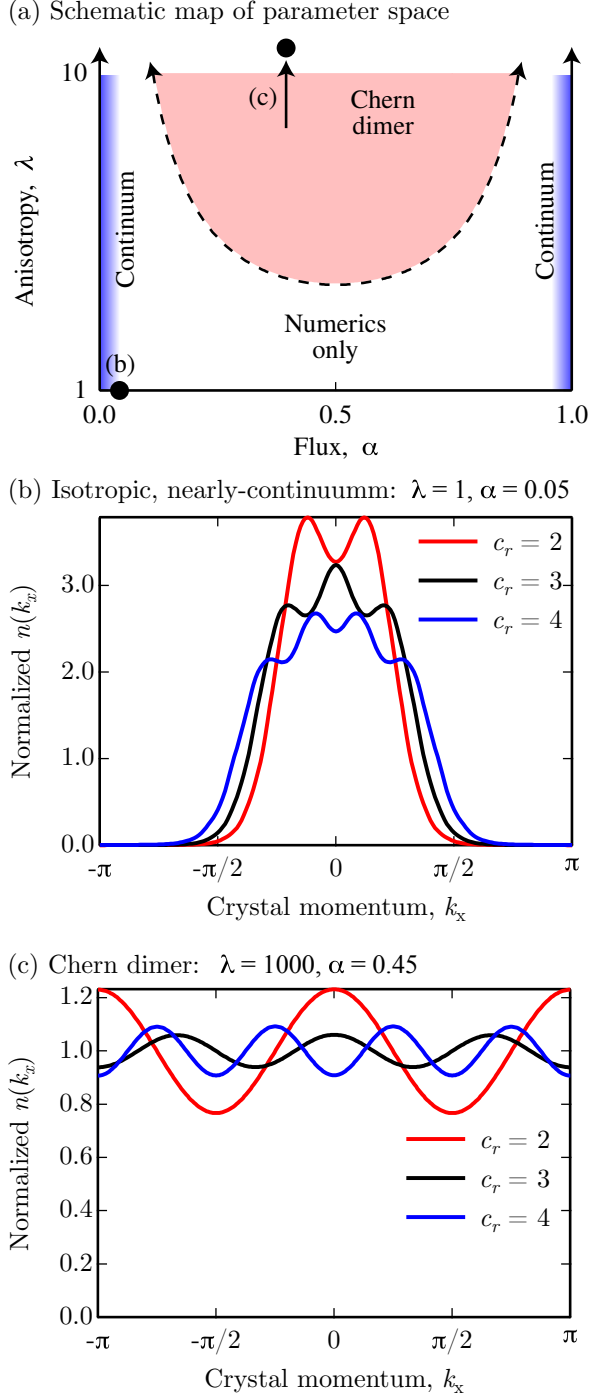


FIG. 1: Link between the Chern number c_r and structure in TOF data as a function of magnetic flux per unit cell α and hopping anisotropy λ . (a) Schematic map of the α - λ plane showing the Chern-dimer and the continuum regimes. In the remainder of parameter space numerics are required. (b,c) Normalized 1D crystal momentum distributions $n(k_x)$, see Eq. (4), computed at three different chemical potentials corresponding to $c_r = 2, 3, 4$; in each case, the number of oscillations is equal to c_r . The data in (b) is for an isotropic $\lambda = 1$ lattice at $\alpha = 0.05$, and the data in (c) is for an anisotropic $\lambda = 1000$ lattice at $\alpha = 0.45$.

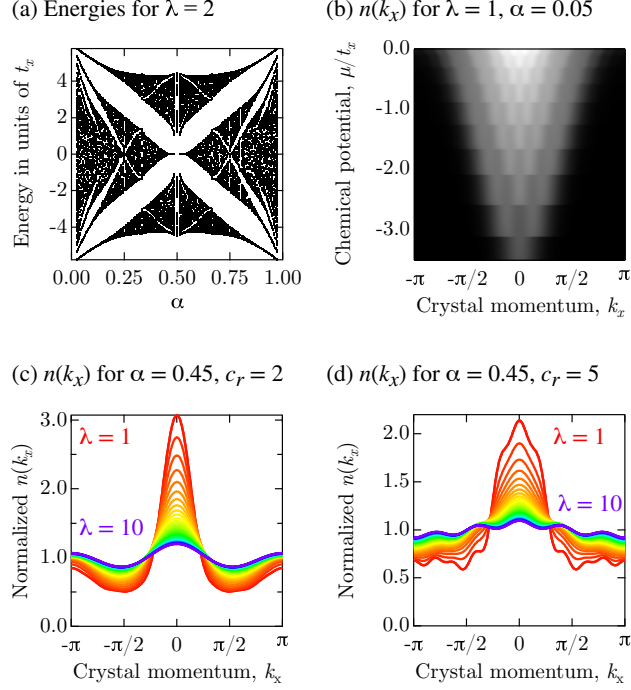


FIG. 2: 1D crystal momentum distributions $n(k_x)$. (a) Energy spectrum of Eqs. (1) and (2) for $\lambda = 2$. (b) Evolution of $n(k_x)$ with increasing chemical potential μ at $\lambda = 1$ and $\alpha = 0.05$ showing c_r increasing in tandem with the number of oscillations in $n(k_x)$. (c,d) Evolution of $n(k_x)$ with increasing anisotropy λ at $\alpha = 0.45$ for (c) $c_r = 2$ and (d) $c_r = 5$. These curves depict the distributions approaching the cosine function with increasing λ .

has $q - 1$ gaps [9]. When the chemical potential μ is inside the r -th energy gap, the system is an integer quantum Hall state with Chern number c_r , defined by the Thouless-Kohmoto-Nightingale-Nijs (TKNN) formula [4] and related to the quantized Hall resistance.

Usually we consider TOF images as approximate representations of the momentum distribution $n(\mathbf{k})$ obtained by imaging the 2D atomic column density after a t_{TOF} period of free expansion. In most cases, the final spatial coordinate of an atom is $\mathbf{x} = \mathbf{v}t_{\text{TOF}}$ where \mathbf{v} is the velocity [12], however, vector potentials complicate the interpretation of TOF images because the velocity is $\mathbf{v} = \hbar\mathbf{k}/m - e\mathbf{A}/m$. In Ref. [13], we showed that suddenly turning the gauge field to zero is equivalent to a brief electric field that takes the initial momentum $\hbar\mathbf{k}$ and maps it to a new final velocity $\mathbf{v}' = \hbar\mathbf{k}/m$. As a result, detected TOF images do approximate momentum distributions [20]. The

crystal momentum distribution

$$\tilde{n}(\mathbf{k}) = \sum_{\mathbf{s}, \mathbf{s}'} \langle f_{\mathbf{s}}^\dagger f_{\mathbf{s}'} \rangle e^{i\mathbf{k} \cdot (\mathbf{s} - \mathbf{s}')}, \quad (3)$$

can be reconstructed from TOF images using the recipe in Ref. [14]. Here, the average $\langle \dots \rangle$ is over the ground state. We also define a 1D crystal momentum distribution by integrating $\tilde{n}(\mathbf{k})$ along \mathbf{e}_y ,

$$n(k_x) = \int_{-\pi}^{\pi} dk_y \tilde{n}(\mathbf{k}). \quad (4)$$

For homogeneous systems, we computed $n(k_x)$ by numerically diagonalizing Eq. (2), while for finite trapped systems we diagonalized Eq. (1). Our numerical results are complemented by analytic analyses for low flux and large anisotropy. In what follows, we discuss in turn the behaviors of $n(k_x)$ in different parameter regimes, starting with an isotropic lattice and low flux.

Figures 1b and 2b show $n(k_x)$ in this isotropic low flux limit, at $\alpha = 0.05$ and $\lambda = 1$. As the chemical potential is increased up to $\mu = 0$, successively higher Hofstadter bands are filled, with Chern numbers $c_r = r$ where $r = 1, 2, 3, \dots$ labels the highest filled band. Correspondingly, $n(k_x)$ has exactly c_r local peaks on top of a smooth envelope, i.e., counting peaks in TOF images unambiguously determines the Chern number, and therefore which quantum Hall state the system is in. To understand this, we recall that for $\alpha \ll 1$, the cyclotron orbit is large compared to the lattice spacing, so the system resembles a free Fermi gas in magnetic field, and the narrow bands in the Hofstadter spectrum map to Landau levels. For r filled Landau levels, $n(k_x)$ is the summed square modulus of the momentum-space wave functions,

$$n(k_x) \propto \sum_{\nu=1}^r (2^\nu \nu!)^{-1} H_\nu^2(k_x \ell_B) e^{-(k_x \ell_B)^2}, \quad (5)$$

where H_ν are the Hermite polynomials, and $\ell_B = \sqrt{\hbar/eB}$ is the magnetic length. Due to the node structure of H_ν , $n(k_x)$ has exactly r local maxima located at the zeros of H_{r+1} . This is reflected in our numerical results as plotted in Fig. 1b for the lattice system. As is depicted by the shaded regions in Fig. 1a, this association is valid in the entire low flux regime and is insensitive to λ .

At larger α the Landau level picture breaks down, but the correspondence between the number of local peaks and the Chern number often persists; Fig. 2c shows examples of $n(k_x)$ for $\alpha = 0.45$ where well resolved peaks do remain even at $\lambda = 1$, but the peaks in Fig. 2d are hardly evident at $\lambda = 1$. More generally, as α increases (for μ residing within the same energy gap), the distinctive features of $n(k_x)$ are generally retained, but compared to the low flux regime, the local peaks

(except at $k_x = 0$) move to higher momenta and can be subsumed into the background structure. The reduction in contrast adds challenge to resolve these peaks in practice.

These often small wiggles on a background turn into regular and pronounced oscillations as the hopping anisotropy λ is increased, regardless of α . Figures 2c and 2d illustrate the progression of $n(k_x)$ from $\lambda = 1$ to $\lambda = 10$, showing pronounced oscillations develop with increasing λ . Most importantly, the simple, universal rule reappears in the limit of $\lambda \gg 1$: the number of oscillations in $n(k_x)$, i.e., the number of peaks for $k_x \in [-\pi, \pi)$, is again exactly equal to the Chern number c_r . As is emphasized in Fig. 1c, $n(k_x)$ asymptotically approaches

$$n(k_x) \propto r \pm \frac{1}{2} \cos(c_r k_x) \quad (6)$$

for chemical potential inside the r -th gap. The one-to-one correspondence, or mapping, between the number of oscillations and the Chern number for anisotropic lattices (Fig. 1a: Chern-dimer regime) is one of our key observations which we now explain analytically.

The $\lambda \gg 1$ limit is tractable in perturbation theory [15] where the solutions to Eq. (2) are simple. When $t_x = 0$ (i.e., $\lambda \rightarrow \infty$), there are q bands each with dispersion $E_r(k_y) = -2t_y \cos(2\pi\alpha r + k_y)$, $r \in \{1 \dots q\}$ (see Fig. 3, where $p = 1$ and $q = 5$). These eigenstates are extended along e_y and localized to single sites as a function of x . As defined in Eq. (2), the r -th band describes states $\psi_{s_x}^r = \delta_{s_x, r}$ localized at site $s_x = r$ and displaced in k_y , as identified in

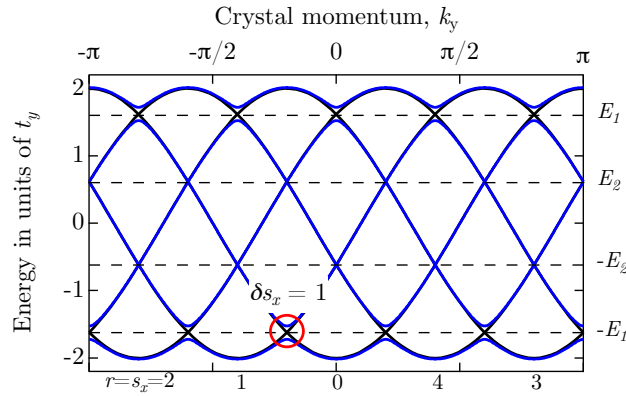


FIG. 3: Energies in the anisotropic limit for $p = 1$, $q = 5$ showing the perfect sinusoidal energies when $\lambda \rightarrow \infty$ (solid black curves), and the avoided crossings when $\lambda = 10$ (solid blue curves). The hybridized states at these crossings correspond to “Chern-dimers,” and the red-circled example has spatial extent $\delta s_x = 1$.

Fig. 3. The bands intersect at numerous degeneracy points k_y^* for states $r = s_x$ and $r' = s'_x$, the spatial separation along \mathbf{e}_x of these localized states is $\ell = s'_x - s_x$. These band-crossing occur at $q - 1$ discrete energies (right axes of Fig. 3) with exactly q crossings having the same ℓ at each energy. For finite λ , t_x hybridizes the states at each crossing, leading to $q(q - 1)$ avoided crossings, and $(q - 1)$ gaps in the band structure. Near each degeneracy point the system is well described by the effective Hamiltonian [15],

$$\check{H}_2(\mathbf{k}) = \Delta_\ell [\cos(k_x \ell) \check{\sigma}_x + \sin(k_x \ell) \check{\sigma}_y] + v_\ell (k_y - k_y^*) \check{\sigma}_z. \quad (7)$$

$\check{\sigma}_{x,y,z}$ are the Pauli matrices in the basis of localized states $|r\rangle$ and $|r'\rangle$; and the k -independent constants are $\Delta_\ell = (-1)^\ell \prod_{R=r+1}^{r'-1} \left\{ \frac{1}{2} [E_r(k_y^*) + E_{r'}(k_y^*)] - E_R(k_y^*) \right\}^{-1}$ and $v_\ell = 2\lambda [\sin(2\pi\alpha r + k_y^*) - \sin(2\pi\alpha r' + k_y^*)]$. The eigenstates are ‘‘Chern-dimers’’, superpositions of $|r\rangle$ and $|r'\rangle$ with wave function

$$\psi_{s_x}^\pm = \frac{1}{\sqrt{2}} (\delta_{s_x, r} + e^{i\beta_\pm} \delta_{s_x, r'}), \quad (8)$$

where $\beta_+ = -\ell(k_x + \pi) + \pi$ and $\beta_- = -\ell(k_x + \pi)$ are relative phases for the upper and lower band edges, respectively. Starting from Eq. (7) it is straightforward to show [15] that the Chern number of each band gap is $c_r = \ell$. For sufficiently anisotropic hopping, dimerized states form at the band edges with spatial extent along \mathbf{e}_x equal to the Chern number of the corresponding gap.

The formation of dimers of size ℓ at the edges of the r -th gap implies that the correlation function

$$C(l) = \sum_{\mathbf{s}} \langle f_{\mathbf{s}}^\dagger f_{\mathbf{s} + l\mathbf{e}_x} \rangle. \quad (9)$$

is peaked at $l = \ell$. For chemical potential in the r -th gap, $C(l)$ asymptotes to a delta function $C(l) \rightarrow \delta(l - \ell) = \delta(l - c_r)$, as $\lambda \rightarrow \infty$. Because $\beta_+ - \beta_- = \pi$ for each crossing, the net contribution to $C(l)$ from dimerized states associated with gaps fully below the Fermi energy is zero. Since $C(l)$ and $n(k_x)$ are a Fourier transform pair, $n(k_x) = \sum_l C(l) \cos(k_x l) / \sqrt{N}$; this yields the $\cos(c_r k_x)$ term in Eq. (6). The contribution from the filled bands below the Fermi energy gives the r offset in Eq. (6).

Finally, we establish a formal connection between $\tilde{n}(\mathbf{k})$ and the Chern number using the Q -matrix [16], a quantity that describes the topology of band structures and plays a fundamental role in the classification of topological insulators. For a homogeneous system with commensurate flux $\alpha = p/q$, we partially Fourier transform Eq. (3), via $f_a(\mathbf{k}) \propto \sum_{\mathbf{S}} \exp[-i\mathbf{k} \cdot (\mathbf{S} + a\mathbf{e}_x)] f_{\mathbf{S} + a\mathbf{e}_x}$; where $\mathbf{S} = \{qn, m\}$ labels the magnetic unit cell, for integer n and m ; $a \in \{1 \dots q\}$ is the

site index within the unit cell; and \mathbf{k} is the crystal momentum within the MBZ. In this notation, $\tilde{n}(\mathbf{k}) = \sum_{ab} \rho_{ab}(\mathbf{k})$ in which $\rho_{ab}(\mathbf{k}) = \langle f_a^\dagger(\mathbf{k}) f_b(\mathbf{k}) \rangle$ is a “momentum distribution matrix” related to the Q -matrix by

$$Q_{ab}(\mathbf{k}) = \delta_{ab} - 2\rho_{ab}(\mathbf{k}). \quad (10)$$

For any band insulator with band structure $E_r(\mathbf{k})$ (with energy measured from the chemical potential), the spectral projection operators $P_+(\mathbf{k})$ and $P_-(\mathbf{k})$ project onto states above or below the chemical potential, respectively. The Q -operator $Q(\mathbf{k}) = P_+(\mathbf{k}) - P_-(\mathbf{k})$ describes a “flattened” Hamiltonian that is smoothly deformed from the original [16]. The crystal momentum distribution is related to the spectral projection operator of the filled bands $\rho(\mathbf{k}) = P_-(\mathbf{k})$, where ρ is related to Q according to Eq. (10). For the asymptotically exact, effective Hamiltonian $\check{H}_2(\mathbf{k})$, the Q -matrix is

$$\check{Q}(\mathbf{k}) = (v_\ell^2 k_y^2 + \Delta_\ell^2)^{-1/2} \check{H}_2(\mathbf{k}). \quad (11)$$

From this we obtain $n(k_x) = q [1 - \text{sign}(\Delta_\ell) \cos(k_x \ell)]$. The cosine dependence on k_x is in agreement with Eq. (6). The Chern number can be calculated from the Q -matrix using the procedure of dimensional reduction [16], and also gives $c_r = \ell$ (in agreement of Ref. [15]).

In contrast with Chern numbers, $n(k_x)$ is not a topologically invariant quantity. Still, the ubiquitous signature of Chern numbers in TOF images makes momentum distributions into an unexpected tool for exploring topological states of matter. In addition to edge states and Hall conductance, ripples in the momentum distribution and dimerized states of anisotropic lattices whose spatial extent encodes the topological quantum numbers provide a new way to characterize and visualize non-trivial topological states. Even for trapped systems or for non-zero temperature the oscillations persist, remaining visible until the temperature significantly exceeds the energy gap of interest. Our study opens the possibility of using momentum distributions to explore other topological states of matter [17] including topological superfluids.

We acknowledge the support of the ONR and NIST (E.Z. and I.I.S), the NRC (N.B.-A.), the NSF through the PFC at JQI (I.B.S.) and the ARO with funds from both the Atomtronics MURI and the DARPA OLE Program (I.B.S).

[1] M. Z. Hasan and C. L. Kane, Rev. Mod. Phys. **82**, 3045 (2010).

[2] X. Qi and S. Zhang, ArXiv:1008.2026 (2010).

- [3] K. v. Klitzing, G. Dorda, and M. Pepper, Phys. Rev. Lett. **45**, 494 (1980).
- [4] D. J. Thouless, M. Kohmoto, M. P. Nightingale, and M. den Nijs, Phys. Rev. Lett. **49**, 405 (1982).
- [5] S. Powell, R. Barnett, R. Sensarma, and S. Das Sarma, Phys. Rev. Lett. **104**, 255303 (2010).
- [6] I. B. Spielman, Phys. Rev. A **79**, 063613 (2009).
- [7] J. Dalibard, G. Juzeliuna, and P. Öhberg, arxiv:1008.5378 (2010).
- [8] Y.-J. Lin, K. Jiménez-García, and I. B. Spielman, Nature **471**, 83 (2011).
- [9] D. R. Hofstadter, Phys. Rev. B **14**, 2239 (1976).
- [10] Y. -J. Lin *et al.*, Nature **462**, 628 (2009).
- [11] N. Goldman *et al.*, Phys. Rev. Lett. **105**, 255302 (2010).
- [12] F. Gerbier, S. Fölling, A. Widera, and I. Bloch, arxiv:0701.420 (2007).
- [13] Y. -J. Lin *et al.*, Nature Physics **advance online publication**, (2011).
- [14] I. B. Spielman, W. D. Phillips, and J. V. Porto, Phys. Rev. Lett. **98**, 080404 (2007).
- [15] E. Fradkin, *Field Theories of Condensed Matter Systems* (Addison Wesley, 1991), pp. 287–292.
- [16] S. Ryu, A. P. Schnyder, A. Furusaki, and A. W. W. Ludwig, New J. of Phys. **12**, 065010 (2010).
- [17] R. N. Palmer, A. Klein, and D. Jaksch, Phys. Rev. A **78** (2008).
- [18] In cold atom experiments the product $e\mathbf{A}$ enters the Hamiltonian, and neither e nor \mathbf{A} is separately defined.
- [19] Estimated assuming a $4E_r$ deep lattice from retro-reflected $\lambda_L = 2d = 800$ nm lasers, giving $t_{x,y} = 0.085E_r$, where the single photon recoil energy is $E_r = \hbar^2/2m\lambda_L^2 = h \times 7.8$ kHz and m is the atomic mass.
- [20] In this context, $n(\hbar\mathbf{k})$ is the *canonical* momentum distribution, not the mechanical momentum distribution.